



# A Readily Implemented Atmosphere Sustainability Constraint for Terrestrial Exoplanets Orbiting Magnetically Active Stars

Evangelia Samara<sup>1,2</sup> , Spiros Patsourakos<sup>3</sup> , and Manolis K. Georgoulis<sup>4</sup> 

<sup>1</sup> Solar-Terrestrial Centre of Excellence, Royal Observatory of Belgium, B-1180 Uccle, Belgium; [evangelia.samara@kuleuven.be](mailto:evangelia.samara@kuleuven.be)

<sup>2</sup> Centre for mathematical Plasma-Astrophysics, Department of Mathematics, KU Leuven, B-3001 Leuven, Belgium

<sup>3</sup> Department of Physics, University of Ioannina, 45110 Ioannina, Greece

<sup>4</sup> Research Center of Astronomy and Applied Mathematics (RCAAM) of the Academy of Athens, 11527 Athens, Greece

Received 2020 December 4; revised 2021 January 31; accepted 2021 February 4; published 2021 March 3

## Abstract

With more than 4300 confirmed exoplanets and counting, the next milestone in exoplanet research is to determine which of these newly found worlds could harbor life. Coronal mass ejections (CMEs), spawned by magnetically active, superflare-triggering dwarf stars, pose a direct threat to the habitability of terrestrial exoplanets, as they can deprive them of their atmospheres. Here we develop a readily implementable atmosphere sustainability constraint for terrestrial exoplanets orbiting active dwarfs, relying on the magnetospheric compression caused by CME impacts. Our constraint focuses on an understanding of CMEs propagation in our own Sun–heliosphere system that, applied to a given exoplanet requires as key input the observed bolometric energy of flares emitted by its host star. Application of our constraint to six famous exoplanets, Kepler-438b, Proxima Centauri b, and Trappist-1d, -1e, -1f, and -1g, within or in the immediate proximity of their stellar host’s habitable zones showed that only for Kepler-438b might atmospheric sustainability against stellar CMEs be likely. This seems to align with some recent studies that, however, may require far more demanding computational resources and observational inputs. Our physically intuitive constraint can be readily and en masse applied, as is or generalized, to large-scale exoplanet surveys to detect planets that warrant further scrutiny for atmospheres and, perhaps, possible biosignatures at higher priority by current and future instrumentation.

*Unified Astronomy Thesaurus concepts:* [Exoplanets \(498\)](#); [Habitable zone \(696\)](#); [Solar flares \(1496\)](#); [Solar coronal mass ejections \(310\)](#); [Stellar coronal mass ejections \(1881\)](#); [Stellar flares \(1603\)](#)

## 1. Introduction

Planets beyond our solar system have become an object of fascination in recent decades, with nearly regular references in headlines and the popular media. Only recently have observational capabilities evolved to the point where potential terrestrial planets are detected around M-type dwarf stars. However, young M-type dwarfs are known to be magnetically active, often more than our middle-aged Sun. Superflares in them are a common occurrence (e.g., Maehara et al. 2012; Armstrong et al. 2016) that should result in fast and massive coronal mass ejections (CMEs; see, e.g., Khodachenko et al. 2007; Lammer et al. 2007; Vidotto et al. 2011, and several others). The CMEs are gigantic, eruptive expulsions of magnetized plasma and helical magnetic fields from the solar and stellar coronae at speeds that may well surpass local Alfvénic and sound speeds, severely but temporarily disrupting stellar winds and generating shocks around their bodily ejecta.

Contrary to solar flares that have been known since the 19th century (Carrington 1859), CMEs were only observed well into the space age (Howard 2006) due to their much fainter magnitude compared to the bright solar photospheric disk. Stellar CME detections are notoriously ambiguous, although recent efforts offer reasonable hope (Argiroffi et al. 2019). However, in strongly magnetized stellar coronae, CMEs are inevitable. In the case of intense stellar magnetic activity and the existence of an atmosphere that shields a planet, extreme pressure effects by CMEs owing to stellar mega-eruptions can, under certain circumstances, cause intense atmospheric depletion via ionization-triggered erosion (e.g., Zendejas et al. 2010). In the solar system, results from NASA’s Mars Atmosphere and Volatile Evolution mission (MAVEN) seem to establish that the sustained eroding effect of solar interplanetary

CMEs (ICMEs) may be responsible for the thin Martian atmosphere (Jakosky et al. 2015) after the planet’s magnetic field weakened.

Our objective here is the introduction of a practical and reproducible (magnetic) atmosphere sustainability constraint (mASC), reflected on a positive, rational number  $\mathcal{R}$  and relying on CMEs and planetary magnetic pressure effects. Here  $\mathcal{R}$  is a dimensionless ratio that, in tandem with the considered habitability zone (HZ; e.g., Kopparapu et al. 2013), can provide an understanding of which terrestrial exoplanets warrant further screening for the existence of a possible atmosphere ( $\mathcal{R} < 1$ ) or otherwise ( $\mathcal{R} > 1$ ). Our mASC becomes fully constrained in the case of tidally locked exoplanets (e.g., Grießmeier et al. 2004) by means of an estimated planetary magnetic field, while if no tidal locking is assumed, the planetary magnetic field can be replaced by a known benchmark field, such as Earth’s. Only magnetic pressure effects are taken into account in this initial study, but our mASC  $\mathcal{R}$  can be generalized at will. Given that pressure effects are extensive and additive, however, adding more terms (i.e., kinetic, thermal) to the CME pressure will only increase the adversity of possible atmospheric erosion effects for a studied exoplanet (e.g., Ngwira et al. 2014).

## 2. (Magnetic) Atmosphere Sustainability Constraint

The magnetic activity of the exoplanets’ host stars reflects on several observational facts, including the bolometric energy of their flares. From it, and assuming a Sun-as-a-star analog further reflected on the solar magnetic energy–helicity (EH) diagram (Tziotziou et al. 2012), we estimate the magnetic helicity of stellar CMEs and a corresponding stellar CME magnetic field based on

the fundamental principle of magnetic helicity conservation in high magnetic Reynolds number plasmas (Patsourakos et al. 2016; Patsourakos & Georgoulis 2017). As explained in Appendix A, CMEs are inevitable in strongly magnetized stellar coronae, as they relieve stars from excess helicity that cannot be shed otherwise.

The near-star CME magnetic field is propagated self-similarly in the astrosphere until it reaches exoplanet orbits (Patsourakos & Georgoulis 2017). The mASC introduced in this study achieves a precise, quantitative assessment of whether the magnetic pressure of stellar ICMEs alone can be balanced by the estimated (tidally locked) or guessed (in the general case) magnetic pressure of observed terrestrial exoplanets at a magnetopause distance large enough to avert the erosion effects of a possible atmosphere.

There are two conceptual pillars of the mASC introduced here. First, it relies on observed stellar flare energies but does not perform a case-by-case stellar eruption analysis. In other words, it does not look at the particular eruption but points to the collective effect of numerous similar eruptions over  $\sim 1$  Gyr, or significant fractions thereof, of the young star's activity (see also Chen et al. 2020). In this sense, the suitable orientation required for an enhanced ICME planeto-effectiveness, namely, the ICMEs' ability to reconnect with the planetary magnetic field causing magnetic storms, is ignored; it is implicitly assumed that numerous such ICMEs will have the correct orientation. Second, our mASC ratio relies explicitly on a worst-case scenario (i.e., largest possible ICME magnetic field strength) magnetic pressure for stellar CMEs ( $\sim B_{\text{worst}}^2$ ) and a best-case scenario planetary magnetic field (i.e., largest possible planetary magnetic field) generated in the planet's core due to internal dynamo action ( $\sim B_{\text{best}}^2$ ). Then, our mASC becomes the ratio of planetary magnetic intensities relating to these pressure terms: the minimum planetary magnetic field (equal to  $B_{\text{worst}}$ ) able to balance the worst-case CME magnetic field and the best-case planetary magnetic field  $B_{\text{best}}$  as per the modeled planetary characteristics, i.e.,

$$\mathcal{R} = \frac{B_{\text{worst}}}{B_{\text{best}}}. \quad (1)$$

The two planetary magnetic field strengths are taken at a critical magnetopause distance from the studied planet in terms of atmospheric erosion effects (Sections 2.1 and 2.2). It is then understood that if  $\mathcal{R} > 1$ , the planet's magnetosphere will be compressed beyond the critical threshold, presumably leading to atmospheric erosion (after processes such as thermal, nonthermal, or hydrodynamic escape, catastrophic erosion, etc., take place; see, for example, Melosh & Vickery 1989; Lundin et al. 2004; Barabash et al. 2007 for more details). Assuming that, statistically, the presumed ICME is not a unique occurrence, the planet may undergo this atmospheric stripping for hundreds of millions of years due to its star's magnetic activity. Magnetic helicity conservation, on the other hand, dictates that at least some (or even most or all) magnetic eruptions in the star will unleash powerful CMEs to shed the excess helicity generated in the star's magnetized atmosphere that is otherwise conserved and remains accumulated in the star's corona. In such situations, one casts doubt on the viability of an atmosphere in the otherwise terrestrial planet, even if the planet is seated well into the HZ of its astrosphere. The opposite is the case for  $\mathcal{R} < 1$ .

### 2.1. The Worst-case CME-equipartition Magnetic Field

A critical magnetopause distance of  $r_{\text{mp}} = 2R_p$  (i.e., two planetary radii, or one radius away from the surface of the planet; see Khodachenko et al. 2007; Lammer et al. 2007) was adopted as the minimum planetocentric distance in which atmospheric ionization and erosion can still be averted during extreme magnetospheric compression. Then, the equipartition planetary magnetic field  $B_{\text{eq}}$  (to be viewed as  $B_{\text{worst}}$ ) that balances the ICME magnetic pressure at  $r_{\text{mp}} = 2R_p$  can be estimated as (see Appendix B for a complete description)

$$B_{\text{eq}} = 8 B_{\text{ICME}}, \quad (2)$$

where  $B_{\text{ICME}}$  is the worst-case ICME axial magnetic field at  $r_{\text{mp}} = 2R_p$ .

To infer  $B_{\text{ICME}}$  at any given astrocentric distance  $r_{\text{ICME}}$ , we first need to constrain the axial magnetic field  $B_0$  of the CME at a near-star distance  $r_0$  (see Appendix A for a derivation). Here  $B_0$  is constrained by observational facts and, more specifically, by assuming a given flux-rope model and a corresponding magnetic helicity formula depending on the radius  $R$  and length  $L$  of the flux rope that can then be solved for  $B_0$  (Patsourakos et al. 2016). Patsourakos & Georgoulis (2017) tested several linear force-free (LFF), nonlinear force-free (NLFF), and non-force-free flux-rope models and determined that the worst-case scenario  $B_0$  for near-Sun CME flux ropes was obtained by the LFF Lundquist flux-rope model (values estimated by other models range between 2% and 80% of the Lundquist values) that gives a magnetic helicity of the form

$$H_m = \frac{4\pi B_0^2 L}{\alpha} \int_0^R J_1^2(\alpha r) r dr, \quad (3)$$

where  $\alpha$  is the constant force-free parameter and  $J_1()$  is the Bessel function of the first kind. Parameter  $\alpha$  is inferred by the additional constraint  $\alpha R \simeq 2.405$ , imposed by the first zero of the Bessel function of the zeroth kind,  $J_0()$ , in the Lundquist model. The flux-rope radius  $R$  corresponds to the CME front that is assumed to have a circular cross section with maximum area.

We use the Lundquist flux-rope model throughout this analysis, as this is a standard ICME model for the inner heliosphere. It gives the strongest near-Sun CME axial magnetic field  $B_0$ , provided that the twist is not excessive (see Patsourakos & Georgoulis 2017). Adopting the fundamental helicity conservation principle for high magnetic Reynolds number plasmas (e.g., Berger 1984) implies a fixed  $H_m$  and dictates that as the CME expands,  $B_0$  decreases self-similarly as a function of  $1/r^2$ , with  $r$  being the heliocentric distance. We maintain this quadratic scaling for distances relatively close to the Sun (e.g., up to the Alfvénic surface, where the solar wind speed matches the local Alfvén speed at  $\sim 10 R_\odot$ ). Beyond that surface, this analysis continues to adhere to helicity conservation but adopts a power-law radial falloff index  $a_B = 1.6$  for the propagation of Lundquist flux-rope solar CMEs within the astrospheres (see Appendix A for a derivation of the exponent). As a result,  $B_{\text{ICME}}$  at a given astrocentric distance  $r_{\text{ICME}}$  is given by

$$B_{\text{ICME}} = B_0 \left( \frac{r_0}{r_{\text{ICME}}} \right)^{1.6}, \quad (4)$$

where  $r_0$  is the near-star distance up to which the CME axial magnetic field scales as  $(1/r^2)$ , and  $B_0$  is this magnetic field at that distance.

## 2.2. The Best-case Planetary Magnetic Field

The “defense” line in the ICME pressure effects for any given planet is being held primarily by the planet’s magnetic pressure. The planet’s dipole magnetic moment  $\mathcal{M}$  gives rise to a planetary magnetic field

$$B_p = \frac{\mathcal{M}}{r_{\text{mp}}^3} \quad (5)$$

for the dayside magnetopause occurring at a planetocentric distance  $r_{\text{mp}}$ . To identify the best-case scenario, we examined several prominent models for the magnetic moment  $\mathcal{M}$  (Busse 1976; Stevenson et al. 1983; Mizutani et al. 1992; Sano 1993; see also Christensen 2010 for a review) to determine which would provide the strongest  $\mathcal{M}$ , focusing particularly on the tidally locked regime. We concluded that an uppercase  $\mathcal{M}$  is provided by Stevenson et al. (1983) and a model variant of Mizutani et al. (1992), namely,

$$\mathcal{M} = \mathcal{M}_{\text{Stev}} \simeq A \rho_c^{1/2} \omega^{1/2} R_c^3 \sigma^{-1/2}. \quad (6)$$

The other models provided values ranging between 18% and 62% of the Stevenson value. In Equation (6),  $A \simeq 3.45 \times 10^5 \text{ A}\cdot\text{s}\cdot\text{kg}^{-0.5}$  is the proportionality constant,  $\omega$  corresponds to the planet’s angular rotation, and  $\rho_c$ ,  $R_c$ , and  $\sigma$  correspond to the planetary core’s mean density, radius, and electrical conductivity, respectively (see Appendix C for more details on the calculations and assumptions made). The  $B_p$  for  $\mathcal{M} = \mathcal{M}_{\text{Stev}}$  (hereafter  $B_{\text{Stev}}$ ) is to be viewed as  $B_{\text{best}}$ .

Summarizing, our mASC ratio of Equation (1) translates to  $\mathcal{R} = (B_{\text{eq}}/B_{\text{Stev}})$ . The  $B_{\text{eq}}$  can be estimated in the case of known bolometric stellar flare energies, while  $B_{\text{Stev}}$  is fully constrained for tidally locked exoplanets.

## 3. Application of the mASC Method

Assuming tidal locking to fully determine  $B_{\text{Stev}}$ , Figure 1 provides the nominal values of  $\mathcal{R}$  for different stellar flare energies and an Earth-like exoplanet lying precisely at the inner (red) and outer (blue) HZ boundary of Kopparapu et al. (2013). This plot represents a different conception of Figure 2 that shows a number of exoplanets provided by the NASA Exoplanet Archive lying within and without both the tidally locked regime and the inner and outer HZ limits. Nevertheless, Figure 1 now includes  $\mathcal{R}$  as a function of stellar flare energies, while stellar masses are implicitly included in the astrocentric distances  $d_{\text{inner}}$  and  $d_{\text{outer}}$ . It comes as no surprise that higher flare energies, statistically resulting in more helical CMEs and stronger axial magnetic fields, require the planet to be orbiting its host star at a larger orbital distance to achieve  $\mathcal{R} < 1$ . For flare energies higher than  $10^{33}$  erg, it appears that planets located precisely on the inner HZ boundary may be incapable of sustaining an atmosphere, while this is the case for energies higher than  $10^{34}$  erg for planets located on the outer HZ boundary.

Importantly, our mASC method can also be applied to case studies of terrestrial exoplanets, provided that flares from their host stars are observed. If these planets are—or are assumed to be—tidally locked, then  $\mathcal{R}$  becomes fully constrained. In Figure 3, we examine six popular cases of terrestrial exoplanets, all within the tidal-locking zone and either within or close to the respective HZ of their host stars. These cases are

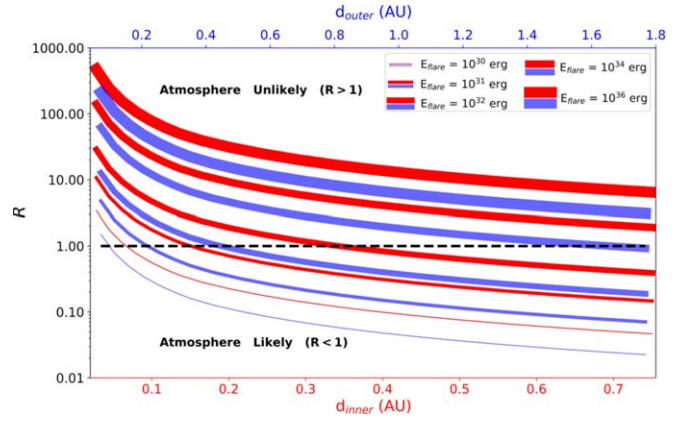


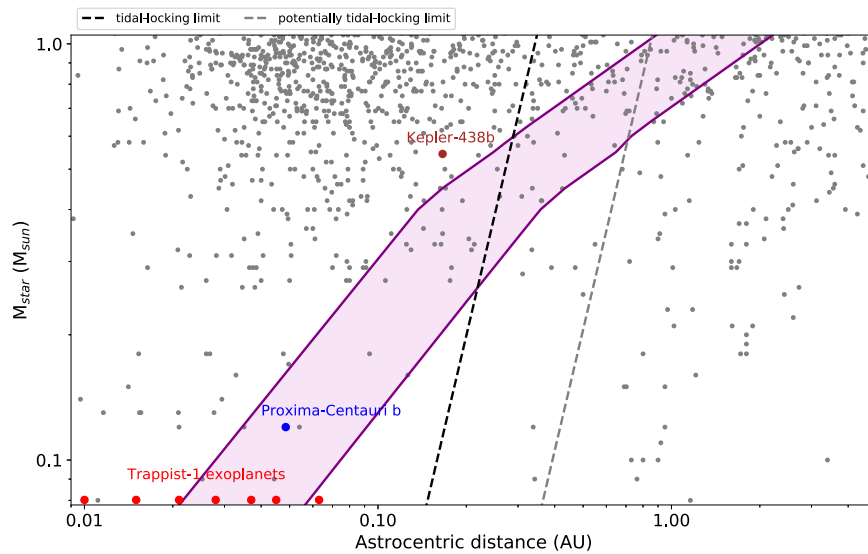
**Figure 1.** The mASC ratio  $\mathcal{R} = (B_{\text{eq}}/B_{\text{Stev}})$  for Earth twins but with different equatorial magnetic fields, lying on the inner (red) and outer (blue) HZ boundary inferred by Kopparapu et al. (2013) for different stellar flare energies, each represented by a different curve thickness. The astrocentric distance in the abscissae implicitly includes the stellar mass shown in Figure 2. The limit  $\mathcal{R} = 1$  (dashed line) separates an apparent nonviability of an atmosphere ( $\mathcal{R} > 1$ ) from an apparently likely atmosphere ( $\mathcal{R} < 1$ ) for both cases.

Kepler-438b (K438b), Proxima Centauri b (PCb), and four Trappist-1 (Tp1) exoplanets, namely, Tp1d, Tp1e, Tp1f, and Tp1g. Actual mASC  $\mathcal{R}$  values and applicable uncertainties (see Appendix D) are provided in Table 1. Figure 3 offers a graphical representation of these results, where observed flare energies from host stars have been taken from Armstrong et al. (2016), Howard et al. (2018), and Vida et al. (2017) for K438b, PCb, and Tp1, respectively.

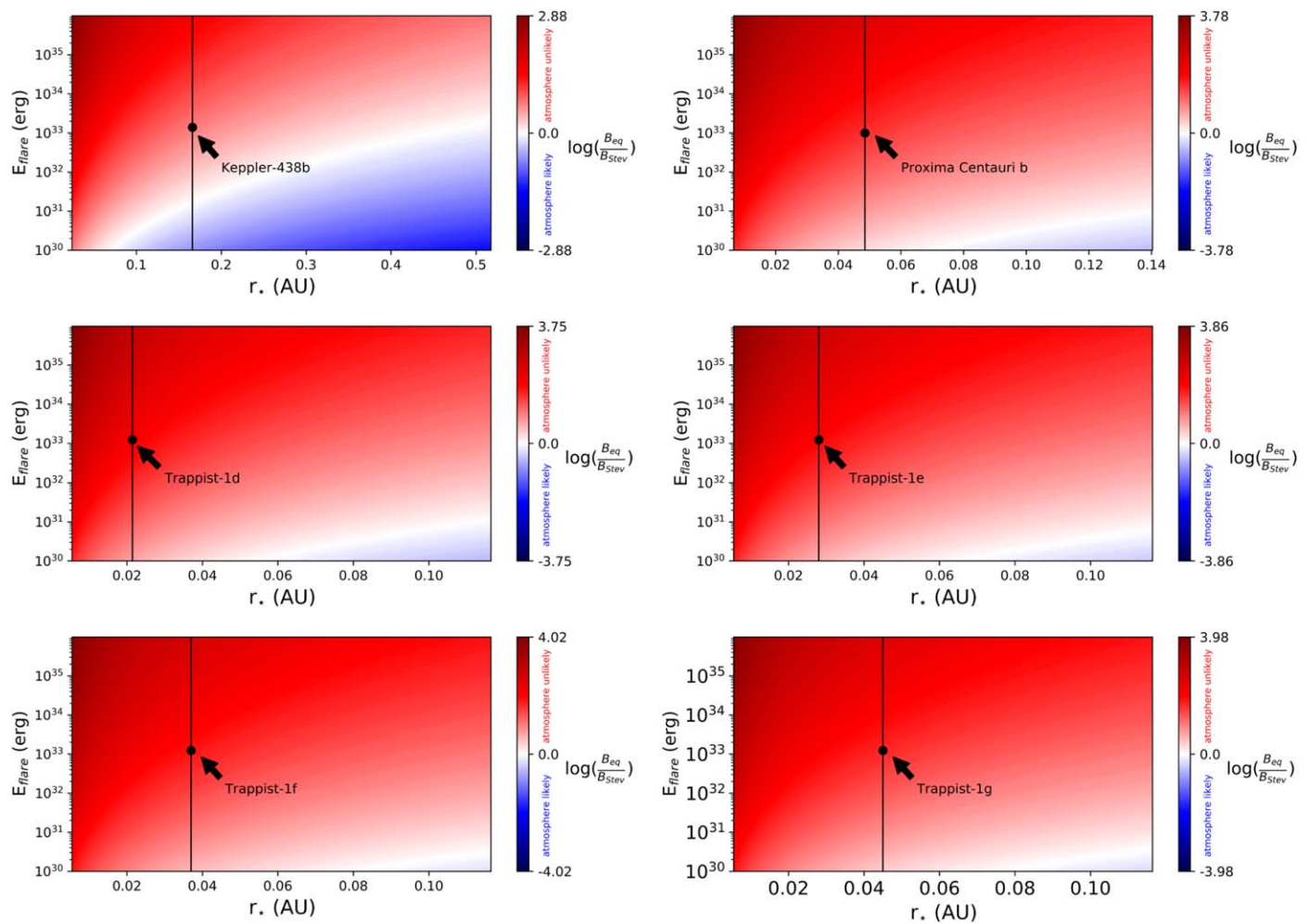
The uncertainty analysis mentioned above and described in Appendix D aims to determine under which circumstances a conclusion of  $\mathcal{R} < 1$  or  $\mathcal{R} > 1$  could be reversed due to applicable uncertainties. In particular, we define an equipartition scaling index  $a_{B(\mathcal{R}=1)}$  for which  $\mathcal{R} = 1$ , along with its uncertainty  $\delta a_B$ . If (i)  $|a_B - a_{B(\mathcal{R}=1)}| > \delta a_B$  for the nominal  $a_B = 1.6$  of Patsourakos & Georgoulis (2016, 2017) or (ii)  $a_{B(\mathcal{R}=1)}$  is steeper than 2 beyond the applicable  $\delta a_B$ , with 2 being the “vacuum” radial falloff index near the star and  $a_B < 2$  reflecting an astrosphere with its own MHD environment, then our conclusion of  $\mathcal{R} < 1$  or  $\mathcal{R} > 1$  is unlikely to change. If the uncertainties are large enough to preclude a safe conclusion, then our main result on an exoplanet is likely to change because of these uncertainties. Analogous uncertainties may be sought in the case of additional pressure effects included in  $\mathcal{R}$ .

Table 1 shows that for all six presumed tidally locked exoplanets, the 1:1 spin-orbit resonance results in planetary rotations that are slow enough to allow  $\mathcal{R} > 1$ , rendering a sustainable atmosphere unlikely. In all cases,  $a_{B(\mathcal{R}=1)}$  is well above the “vacuum” value of 2, with PCb and the four Tp1 exoplanets showing  $a_{B(\mathcal{R}=1)} > 2$  beyond the applicable uncertainties. Hence, for five out of six potentially tidally locked exoplanets, our result for  $\mathcal{R} > 1$ , meaning a nonsustainable atmosphere, seems robust. The result could be reversed for K438b, as the difference between  $a_{B(\mathcal{R}=1)}$  and 1.6 is within the applicable uncertainties, meaning that if  $a_B$  systematically lies in the range (1.6, 2.0), then the exoplanet might conceivably sustain an atmosphere.

The above underlines the potential value of the mASC  $\mathcal{R}$ , even in its simplest form involving only magnetic pressure effects; lying in the HZ of their host stars does not necessarily make exoplanets capable of sustaining an atmosphere, a favorable Earth Similarity Index (ESI; Schulze-Makuch et al. 2011) notwithstanding. This



**Figure 2.** Ensemble of 1771 confirmed exoplanets by the NASA Exoplanet Archive plotted on a diagram of stellar mass vs. astrocentric distance. We restrict the analysis to stars less or equally as massive than the Sun, while the exoplanets shown have a confirmed orbital semimajor axis. Inner and outer HZ limits are indicated by solid lines enclosing the pink shaded HZ area, while the black and gray dashed lines indicate internal and potential external tidal-locking limits, respectively. The locations of nine exoplanets, six of which are studied here due to their proximity to or presence within the HZ, are also highlighted.



**Figure 3.** Testing the viability of a potential atmosphere from the value of the mASC  $\mathcal{R}$  for six confirmed exoplanets, namely (clockwise from top left), K438b, PCb, Tp1e, Tp1g, Tp1f, and Tp1d. Ordinates correspond to stellar flare energies and abscissae to astrocentric distances. The color scales correspond to  $\log(\mathcal{R})$ . Each planet is represented by a point corresponding to coordinates set by the maximum observed flare energies from its host star and confirmed orbital distances, highlighted by vertical lines.

**Table 1**  
Six Case Studies of the mASC  $\mathcal{R}$  Value as Depicted in Figure 3

Exoplanet	Abridged	$\mathcal{R}$	Atmosphere Likely?	$a_{B(\mathcal{R}=1)}$	$\delta a_B$	Result Robust?
Kepler-438b	K438b	5.46	No	2.48	0.99	No
Proxima Centauri b	PCb	42.84	No	3.48	0.96	Yes
Trappist-1d	Tp1d	95.35	No	4.95	1.40	Yes
Trappist-1e	Tp1e	77.87	No	4.24	1.15	Yes
Trappist-1f	Tp1f	70.61	No	3.80	0.99	Yes
Trappist-1g	Tp1g	48.53	No	3.43	0.90	Yes

**Note.** The values of  $\mathcal{R}$  corresponds to our nominal radial power-law falloff index  $a_B = 1.6$ . The index  $a_{B(\mathcal{R}=1)}$  corresponds to the equipartition  $a_B$  value for which  $\mathcal{R} = 1$ , while  $\delta a_B$  corresponds to the uncertainty of  $a_{B(\mathcal{R}=1)}$ . The last column assesses whether our result is robust as per the difference  $a_{B(\mathcal{R}=1)} \pm \delta a_B$  from the nominal  $a_B$  value.

would be the case for PCb and Tp1d, e, f, and g, although virtually all lie in the HZ. Conversely, K438b is slightly beyond the inner HZ that might inhibit an atmosphere and possible liquid water on its surface, but at the same time, due to its larger orbital distance, it might be relatively immune to at least plausible, as per flare observations, space weather from its host star.

#### 4. Conclusions

This versatile and highly reproducible analysis shows that space weather cannot be left out of considerations for planetary habitability in stellar systems (Airapetian et al. 2020). It carries both value and promise; consider the European Space Agency CHAracterising ExOPlanet Satellite (CHEOPS) mission, for example (e.g., Sulis et al. 2020). The mission is designed to characterize only selected, confirmed exoplanets, ranging from super-Earth to Neptune sizes, aiming toward studies that extend into their potential atmospheres. Although the mission is already in orbit, analyses such as this could help assess future observing priorities. The same applies to optimizing exoplanet selection for biosignature analysis in the framework of the upcoming James Webb mission.

In anticipation of these exciting observations that will give the ultimate test of our method, we hereby supply a first round of tentative tests aiming toward its validation. For example, it was recently shown that LHS 3844b (Vanderspek et al. 2019; Kane et al. 2020), a rocky exoplanet orbiting an M dwarf star within its tidally locked zone, lacks an atmosphere. Kane et al. (2020) suggested that the mother star of LHS 3844b exhibited an active past, comparable to that of Proxima Centauri. By adopting, therefore, a maximum superflare energy identical to the one of Proxima Centauri, we obtained  $R = 251.08$  ( $>1$ , atmosphere unlikely), which agrees with the observations. Also, our result seems robust because  $|a_B - a_{B(\mathcal{R}=1)}| > \delta a_B$ .<sup>5</sup> Our mASC could be indirectly validated as well by checking if other studies—also focusing on tidally locked, terrestrial worlds and having similar objectives—converge on similar results. This said, the results presented here are in qualitative agreement with MHD simulations of stellar winds, for example, by Garraffo et al. (2017), that find extreme magnetospheric compressions below  $\approx 2.5$  planetary radii for Tp1d–g and a magnetopause distance of [1.5, 4.5] planetary radii for PCb. Recent extensive (and

computationally expensive) MHD models of stellar CMEs (e.g., Lynch et al. 2019), along with semiempirical approaches (e.g., Kay et al. 2016), have emerged, and both approaches take as input maps the stellar surface magnetic field inferred by Zeeman–Doppler imaging reconstructions (e.g., Donati & Brown 1997). While detailed, these studies may be rather impractical for bulk application to a large number of exoplanets. On the other hand, our introduced mASC could provide guidance to large-scale MHD simulations of stellar CMEs by efficiently scanning and bracketing the corresponding parameter space so that the simulations could be performed only for pertinent cases.

Concluding, we reiterate that mASC  $\mathcal{R}$  can be generalized at will with additional pressure terms, albeit mainly from the ICME side. In its most general form,  $\mathcal{R} = P_{\text{eq}}/P_{\text{planet}}$ , with worst- and best-case scenario pressure terms  $P_{\text{eq}}$  and  $P_{\text{planet}}$ , respectively. We note, in particular, the study of Moschou et al. (2019), where a (flare) energy versus (CME) kinetic energy diagram is inferred from stellar observations and modeling. Such statistics could be integrated into the EH diagram of this study to revise the  $P_{\text{eq}}$  term. The EH diagram used here is also an entirely solar one, so any possibilities of extending it to better reflect the magnetic activity of dwarf, planet-prolific stars are well warranted. Equally meaningful  $P_{\text{planet}}$  terms could be introduced to provide a far more sophisticated but still readily achieved mASC ratio  $\mathcal{R}$  for the screening of alien terrestrial worlds for potential atmospheres and, ultimately, life.

The authors would like to thank the anonymous referee for comments and suggestions that improved the manuscript. This work was inspired by and originated during the M.Sc. thesis of E.S., implemented at the University of Athens and the Research Center for Astronomy and Applied Mathematics of the Academy of Athens, Greece. We thank both institutions for their support and encouragement. The authors would also like to extend their acknowledgments to Prof. Dr. Stefaan Poedts from the Centre for mathematical Plasma-Astrophysics (CMPA), Department of Mathematics, KU Leuven, for his support and encouragement on this work.

*Facilities:* The properties of the exoplanets and host stars used in this study are available at the NASA Exoplanet Archive (<https://exoplanetarchive.ipac.caltech.edu/>).

*Software:* The code to implement the mASC for any terrestrial-like exoplanet lying within the tidally locked regime of its host star is available in the following repository: <https://github.com/SamaraEvangelia/mASC-method>.

<sup>5</sup> For this specific exoplanet, which orbits very close to its mother star, we maintain the quadratic scaling of  $B_0$  with astrometric distance ( $1/r^2$ ) for distances up to  $7 R_*$  and not  $10 R_*$ . Beyond  $7 R_*$ , we adopt the same power-law radial falloff index  $a_B = 1.6$  for the propagation of Lundquist flux-rope solar CMEs within the astrospheres.

## Appendix A Near-Sun/Star CMEs and Helio-/Astrospheric Propagation

A physically meaningful expression of magnetic helicity in the Sun and magnetically active stars is the relative helicity, related to the absence of vacuum and hence the flow of electric currents in the solar and stellar coronae, along with the topological settings of solar (and stellar) magnetic fields that are only partially observed and detected, on and above the stars' surface. By construction, the relative helicity must be quantitatively connected to the excess or free magnetic energy that is also explicitly due to the presence of electric currents (e.g., Sakurai 1981). An attempt to correlate the free magnetic energy with the relative magnetic helicity in solar active regions was made by Georgoulis & LaBonte (2007) for LFF magnetic fields and Georgoulis et al. (2012) for NLFF ones.

The NLFF (magnetic) energy–(relative) helicity correlation resulted in the EH diagram of Tziotziou et al. (2012). There,  $\sim 160$  vector magnetograms of observed solar active regions were treated in the homogeneous way of Georgoulis et al. (2012), aiming toward a scaling between the NLFF free magnetic energy  $E_c$  and relative helicity  $H_m$ . They found a robust scaling of the form (cgs units)

$$\log|H_m| \propto 53.4 - 0.0524(\log E_c)^{0.653} \exp \frac{97.45}{\log E_c}. \quad (\text{A1})$$

Here  $|H_m|$  refers to the magnitude of the relative helicity  $H_m$ , which can be right- (+) or left- (–) handed. A similar expression to Equation (A1) provides a simpler power-law dependence between  $|H_m|$  and  $E_c$  of the form (cgs units)

$$|H_m| \propto 1.37 \times 10^{14} E_c^{0.897}. \quad (\text{A2})$$

The above EH scaling was shown to hold for typical active-region free energies in the range  $E_c \sim (10^{30}, 10^{33})$  erg and respective relative helicity budgets  $|H_m| \sim (10^{40}, 10^{44})$  Mx<sup>2</sup>. The robustness of the EH diagram scaling was validated in multiple cases that involved not only active regions but also quiet-Sun regions and MHD models (Tziotziou et al. 2013).

Combining the EH scaling with the conservation principle of the relative magnetic helicity,  $E_c$  in Equations (A1) and (A2) is dissipated in every instability (solar flare, CME, etc.), while  $H_m$  is only shed away from the Sun via CMEs. If an active region was to completely relax (i.e., return to the vacuum energy state) by a single magnetic eruption, then for a given free magnetic energy  $E_c$ , it would expel helicity  $H_m$ . This is the core reasoning behind a worst-case scenario solar eruption originating from a given solar source. Typically, up to  $\sim 10\%$  of the total free energy and up to 30%–40% of the total magnetic helicity of the source are dissipated and ejected, respectively, in a solar eruption (see, e.g., Nindos et al. 2003; Moraitis et al. 2014).

The majority of CME ejecta are observed to be in the form of a magnetic flux rope (e.g., Vourlidis et al. 2013, 2017), with this geometry surviving the CMEs' inner heliospheric propagation all the way to the Sun–Earth libration point L1 and probably beyond (e.g., Zurbuchen & Richardson 2006; Nieves-Chinchilla et al. 2018). Based on the flux-rope CME geometry, tools such as the graduated cylindrical shell (GCS) model of Thernisien et al. (2009) and Thernisien (2011) processed observations by the STEREO/SECCHI coronagraph (Howard et al. 2008) to obtain the aspect ratio  $k = R/L$  between the radius  $R$  and along with the half-angular width  $w$  of the CME

flux rope at some distance (typically,  $10 R_\odot$ ) away from the Sun. The length  $L$  corresponds to the perimeter of the flux rope, while the radius  $R$  corresponds to the CME front, which is assumed to have a circular cross section with maximum area.

The worst-case scenario  $B_0$  for near-Sun CME flux ropes was provided by the LFF Lundquist flux-rope model, which was used throughout this analysis and gives a magnetic helicity of the form

$$H_m = \frac{4\pi B_0^2 L}{\alpha} \int_0^R J_1^2(\alpha r) r dr, \quad (\text{A3})$$

where  $\alpha$  is the constant force-free parameter and  $J_1()$  is the Bessel function of the first kind. Parameter  $\alpha$  is inferred by the additional constraint  $\alpha R \simeq 2.405$ , imposed by the first zero of the Bessel function of the zeroth kind,  $J_0()$ , in the Lundquist model.

As already mentioned, for helicity conservation imposing a fixed  $H_m$ , the Lundquist model requires that as the CME expands,  $B_0$  decreases self-similarly as a function of  $1/r^2$  for distances close to the Sun. In this analysis, however, and for distances away from the Sun (see also Patsourakos & Georgoulis 2016), the self-similar expansion was not a priori assumed to be quadratic (i.e.,  $1/r^2$ ), but more generally,  $(1/r^{a_B})$ , with  $a_B$  being the absolute value of the power-law radial falloff index. This different index, still under helicity conservation that dictates the respective power laws for the increase (expansion) of the CME flux rope  $R$  and  $L$ , aimed to include all effects present during heliospheric propagation and the interaction of ICMEs with the ambient solar wind (see, e.g., Manchester et al. 2017, for an account of these effects). Prominent among them is the CME flattening (see, e.g., Raghav & Shaikh 2020, and references therein) that tends to distort the CME geometry due to plasma draping or flux pileup as the CME pushes through the heliospheric spiral. As a result, inner heliospheric propagation implies that  $B_{\text{ICME}}$  at a given heliocentric distance  $r_{\text{ICME}}$  is given by

$$B_{\text{ICME}} = B_0 \left( \frac{r_0}{r_{\text{ICME}}} \right)^{a_B}, \quad (\text{A4})$$

where  $r_0$  is the (near-Sun) distance up to which the CME axial magnetic field scales as  $(1/r^2)$ , and  $B_0$  is this magnetic field at that distance.

This analysis adopts  $a_B = 1.6$  in Equation (A4) for the propagation of Lundquist flux-rope stellar CMEs within their astrospheres (where  $a_B$  can vary in the range [1.34, 2.16]; see Salman et al. 2020). A Monte Carlo simulation for various stellar ( $k, w$ ) pairs is adopted, while the stellar CME  $|H_m|$  is inferred by the bolometric observed stellar flare energies via Equation (A2). A valid question is where in the near-star space are we to apply the model ( $k, w$ ) that was taken at  $10 R_\odot$ ; assuming a  $10 R_*$  astrocentric distance, where  $R_*$  is the radius of the host star, we should apply a “fudge-factor” correction to  $B_0$  as follows:

$$B_{0(10 R_*)} = B_{0(10 R_\odot)} \left( \frac{R_\odot}{R_*} \right)^2. \quad (\text{A5})$$

This factor is adopted for the cases of this study's six exoplanets and their host stars. In the general case, or where no assessment is taken for the stellar radius, one may start the astrospheric propagation at a physical astrocentric distance of  $10 R_\odot$ ,

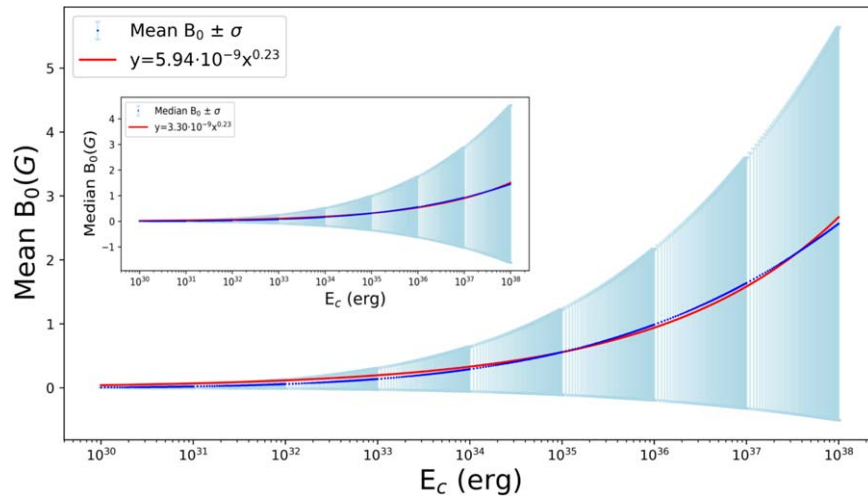


**Figure 4.** Mean (main plot) and median (inset) values of the near-star CME axial magnetic field  $B_0$  at a physical distance of  $10 R_{\odot}$  from the star. The modeled data are shown by blue points, while the least-squares power-law best fits are shown by red curves. Standard deviations around each  $B_0$  value are represented by cyan ranges.

independently from the stellar radius (provided, of course, that this radius does not exceed  $10 R_{\odot}$ ).

Figure 4 provides the mean  $B_{0(10 R_{\odot})}$  of the abovementioned Monte Carlo simulation for different flare energies  $E_c$ , along with a standard deviation around these values (cyan ranges). The inset in Figure 4 provides the respective median values. We notice that both mean and median  $B_{0(10 R_{\odot})}$  can be adequately modeled by power laws of the flare energy  $E_c$  of the form

$$B_{0(10 R_{\odot})} (G) = f E_c^{0.23} (\text{erg}), \quad (\text{A6})$$

where the proportionality constant  $f$  is  $3.30 \times 10^{-9}$  (median) or  $5.94 \times 10^{-9}$  (mean), with an uncertainty amplitude  $1.29 \times 10^{-8}$ .

## Appendix B ICME Equipartition Magnetic Field

Figure 5 provides the worst-case scenario axial magnetic field of ICME magnetic flux ropes (as virtually all CMEs/ICMEs are expected to be) as a function of solar/stellar flare energies and helio-/astrocentric distances. The ICME magnetic pressure effects on the planet will be determined from this magnetic field strength.

Textbook physics dictates that either nominal solar/stellar winds or “stormy” ICMEs exert pressure that comprises magnetic (i.e.,  $B^2/(8\pi)$ ), kinetic (i.e., ram;  $\rho v^2$ ), and thermal (i.e.,  $n k T$ ) terms as per the local MHD environment (plasma number density, mass density, and speed,  $n$ ,  $\rho$ , and  $v$ , respectively, and magnetic field  $B$ ). At the planet’s dayside at few to several planetary radii, the only nonnegligible pressure term is magnetic pressure stemming from the planetary magnetosphere. This is because a possible atmosphere typically wanes at the planetary thermosphere or exosphere, already at small fractions of a planetary radius. In a seminal early work, Chapman & Ferraro (1930) considered a spherical magnetosphere interfacing with interplanetary ejecta. Adopting this working hypothesis and taking only the magnetic pressure term of the ICME determined by its characteristic field  $B_{\text{ICME}}$ , the existence of a magnetopause at planetocentric distance  $r_{\text{mp}}$  implies an equilibrium of the form

(Patsourakos & Georgoulis 2017)

$$\frac{B_{\text{ICME}}^2}{8\pi} = \frac{B_{\text{mp}}^2}{8\pi} \left( \frac{1}{r_{\text{mp}}} \right)^6, \quad (\text{B1})$$

where  $r_{\text{mp}}$  is expressed in planetary radii and  $B_{\text{mp}}$  is the planetary magnetic field at the magnetopause. We now adopt a critical magnetopause distance, that is, the minimum planetocentric distance at extreme compression in which atmospheric ionization and erosion can still be averted at  $r_{\text{mp}} = 2 R_p$  (i.e., two planetary radii, or one radius away from the surface of the planet). This is a limit already adopted by several previous studies (Khodachenko et al. 2007; Lammer et al. 2007). Therefore, the equipartition planetary magnetic field  $B_{\text{eq}}$  that balances the ICME magnetic pressure at  $r_{\text{mp}} = 2 R_p$  is

$$B_{\text{eq}} = 8 B_{\text{ICME}} \quad (\text{B2})$$

from Equation (B1). This equipartition field for the same range of flare energies and astrocentric distances (viewed in this case as the exoplanets’ mean orbital distances in circular orbits) as in Figure 5 is provided in Figure 6. Equation (B2) and Figure 6, therefore, provide the requirement for the planetary magnetic field such that planets avoid atmospheric erosion due to a given ICME magnetic pressure.

It would worth mentioning at this point that the toroidal component of the interplanetary magnetic field could become important in the case of fast rotators such as M stars (e.g., Petit et al. 2008; Kay et al. 2016; Villarreal D’Angelo et al. 2019). In such a case, an extra term is added in the pressure-balance equation at the substellar point. However, we note that in the case of active M dwarf stars, the notion of a Parker spiral for the associated interplanetary magnetic field may not be fully applicable, given the much more frequent CME activity than in the solar case that could keep the spiral significantly perturbed virtually at all times.

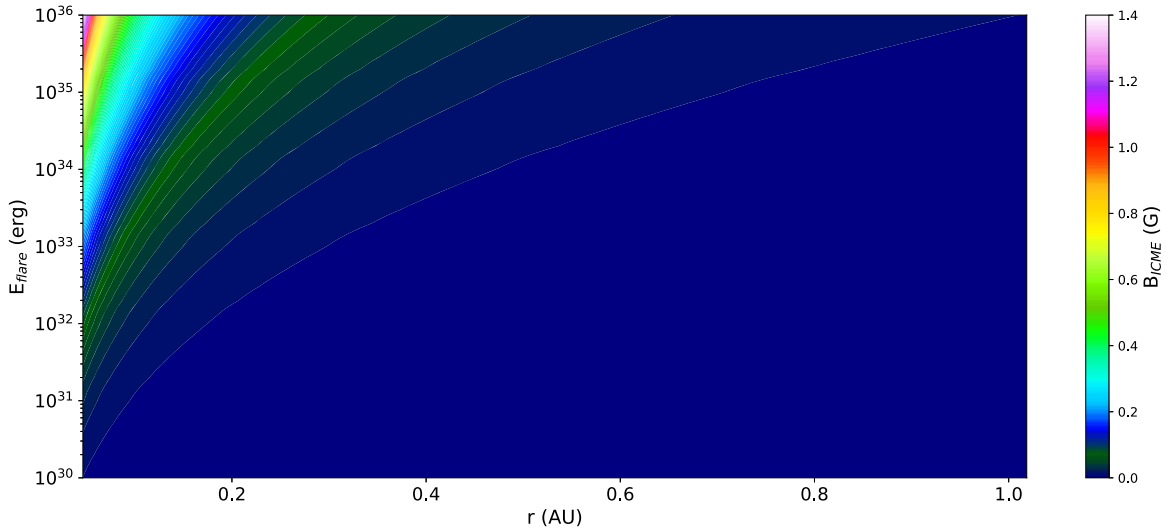


**Figure 5.** Worst-case scenario axial magnetic field for ICME magnetic flux ropes as a function of source flare energy and astrocentric distance, up to 1 au. A wide range of flare energies is provided, from flares observed on the Sun (i.e., up to  $10^{33}$  erg) to orders-of-magnitude stronger superflares with energies up to  $10^{36}$  erg.

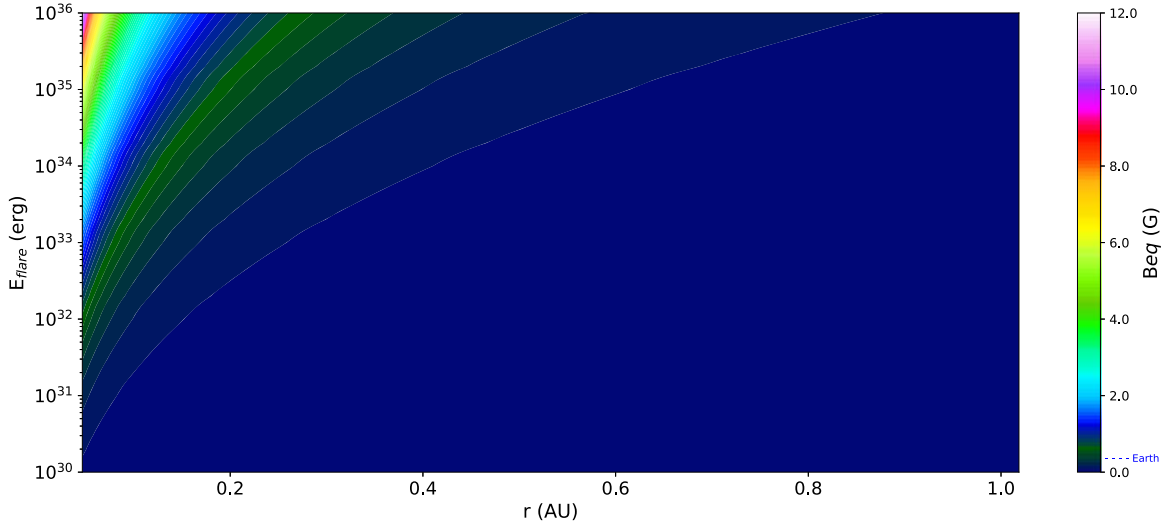


**Figure 6.** Same as Figure 5 but showing the equipartition magnetic field of the planet at the adopted atmospheric erosion critical threshold of two planetary radii. The label “Earth” in the color bar shows the uncompressed terrestrial equatorial magnetic field for reference.

### Appendix C

#### Best-case Planetary Magnetic Field in Tidally Locked Regimes

The planet’s dipole magnetic moment  $\mathcal{M}$  gives rise to a planetary magnetic field

$$B_p = \frac{\mathcal{M}}{r_{mp}^3} \quad (\text{C1})$$

for the dayside magnetopause occurring at a planetocentric distance  $r_{mp}$ . The magnetic moment and resulting magnetic field in exoplanets are generally unknown, and one may need to use a known planetary field benchmark (i.e., Earth’s or another) to estimate the equilibrium magnetopause (or standoff) distance between a planet and the stellar wind it encounters. For Earth, in particular, this distance is  $\sim 10 R_{\oplus}$  for the unperturbed solar wind, where  $R_{\oplus}$  is Earth’s radius. Patsourakos & Georgoulis (2017) concluded that the terrestrial magnetopause cannot be compressed to a value smaller than  $\sim 5 R_{\oplus}$  by the magnetic

pressure of ICMEs, an estimate that aligns with other findings of extreme magnetospheric compression (e.g., Russell et al. 2000).

While our knowledge of exoplanet magnetic fields is virtually nonexistent, for the subset of exoplanets that lie in the tidally locked zone of their host stars (Grießmeier et al. 2004; Khodachenko et al. 2007), we have an additional constraint: the 1:1 spin–orbit resonance (see Figure 2 to visually locate all such exoplanets). It implies that tidally locked exoplanets have a self-rotating speed equal to the rotational speed around their host stars in a synchronous rotation. While exceptions are possible, this study adopts the 1:1 spin–orbit resonance because it affords us an estimate of the angular self-rotation of the planet in case the orbital period around its host star is known from observations. Synchronous rotation statistically weakens the planetary magnetic dipole moment, but at the same time, it enables its first-order estimation, further enabling an estimation of the planetary magnetic field that is crucial for this analysis. In the case of

planets that are not tidally locked to their mother star, or we do not employ tidal locking, the planetary magnetic field ( $B_{\text{best}}$ ) will have to be hypothesized by assigning an ad hoc magnetic dipole moment in Equation (C1). No scaling law is employed then, but we can use a benchmark planetary field, such as Earth's, for example.

Emphasizing the terrestrial planets, we calculate the upper-case  $\mathcal{M}$  provided by the Stevenson et al. (1983) model by assuming a core conductivity  $\sigma = 5 \times 10^5 \text{ S m}^{-1}$  as per Stevenson (2003). The mean core density  $\rho_c$  that enters the relationship is further assumed to be equal to the mean density of the planet, i.e.,  $\rho_c = \rho = 3M_p/(4\pi R_p^3)$ , where  $M_p$  and  $R_p$  are the planetary mass and radius, respectively. The assumption allows a density estimate based on direct or implicit observational facts relevant to the terrestrial planet under study. Moreover, an angular rotation ( $\omega$ ) equal to the planet's angular rotation around its host star is adopted for presumed tidally locked planets. In the case of planets that are not tidally locked, as explained initially, ad hoc planetary field benchmarks must be used.

Another obvious unknown is the planetary core radius,  $R_c$ . For Earth, we have  $R_c \simeq 0.55 R_{\oplus}$ , while for Mercury, the fraction is significantly larger ( $R_c \simeq 0.85 R_{\text{g}}$ ). Regardless, an upper limit of  $R_c$  is the radius of the studied planet. In the frame of adopting the best-case scenario for the planetary magnetic pressure, we will use this upper limit, adopting  $R_c = R_p$ . As an example, the above settings and Equation (6) for Earth imply an equatorial magnetic field of  $\sim 0.309 \text{ G}$ , almost identical to the nominal terrestrial equatorial field of  $\sim 0.305 \text{ G}$ .

### Appendix D Sensitivity Analysis

As already explained, we are essentially interested in the ratio  $\mathcal{R} = B_{\text{eq}}/B_{\text{Stev}}$  of the equipartition magnetic field  $B_{\text{eq}}$  of a planet at magnetopause distance  $r_{\text{mp}} = 2R_p$  to the expected upper-limit Stevenson magnetic field ( $B_{\text{Stev}}$ ) for the planet. This paragraph details our approach to determine whether applicable uncertainties are capable of changing the outcome of  $\mathcal{R} > 1$  or  $\mathcal{R} < 1$  for a given exoplanet.

We start by asking what value of the radial falloff power-law index  $a_B$  is required for  $\mathcal{R} = 1$ . Under this condition and Equation (4), we find

$$a_{B(\mathcal{R}=1)} = \frac{\log(B_{\text{Stev}}/(8 B_0))}{\log(r_0/r_{\text{ICME}})}. \quad (\text{D1})$$

Evidently, if we find  $\mathcal{R} > 1$  for the nominal  $a_B = 1.6$ , then  $a_{B(\mathcal{R}=1)} > a_B$ , meaning that the ICME magnetic field must decay more abruptly than assumed to achieve  $\mathcal{R} = 1$  at  $2R_p$ . The opposite is the case if we find  $\mathcal{R} < 1$  for  $a_B = 1.6$  (i.e.,  $a_{B(\mathcal{R}=1)} < a_B$ ).

Let us now assume an uncertainty  $\delta B_0$  of the near-star magnetic field of the CME,  $B_0$ . This relates to the uncertainty  $\delta a_B$  on  $a_{B(\mathcal{R}=1)}$  as follows:

$$\frac{\delta a_B}{a_{B(\mathcal{R}=1)}} = \frac{1}{\ln(8B_0/B_{\text{Stev}})} \frac{\delta B_0}{B_0}. \quad (\text{D2})$$

From Equation (A3), we can relate  $\delta B_0$  to the uncertainty in the CME helicity,  $\delta H_m$ , as

$$\frac{\delta H_m}{|H_m|} = 2 \frac{\delta B_0}{B_0}, \quad (\text{D3})$$

and by using the EH diagram of Equation (A2), we can find another expression for  $\delta H_m$ , namely,

$$\frac{\delta H_m}{|H_m|} = \left[ \beta^2 \left( \frac{\delta E_c}{E_c} \right)^2 + (\ln E_c)^2 \delta \beta^2 \right]^{1/2} \simeq \ln E_c \delta \beta, \quad (\text{D4})$$

for  $(\delta E_c/E_c) \lesssim 4$  and typical superflare energies  $E_c \geq 10^{30} \text{ erg}$ . In Equation (D4), we have propagated the uncertainties for the free energy of the eruptive flare,  $\delta E_c$ , and the power-law index in the EH diagram of Equation (A2),  $\delta \beta \simeq 0.05$ . In Equation (D3), we have further assumed that the forward-modeled GCS geometrical properties  $R$  and  $L$  of the CME carry no uncertainties, as even when assuming  $(\delta k/k) = (\delta w/w) = 1$ , the dominant error term is still  $(\delta B_0/B_0)$ . As further shown in Equation (D4), given the term depending on the logarithm of  $E_c$ , we may ignore the contribution of  $\delta E_c$  for typical superflare energies  $E_c \in (10^{30}, 10^{38}) \text{ erg}$ , thus simplifying the uncertainty equation.

Combining Equations (D3) and (D4), we eliminate  $(\delta H_m/|H_m|)$  and solve for  $\delta B_0$  to find

$$\frac{\delta B_0}{B_0} \simeq \frac{1}{2} \ln E_c \delta \beta. \quad (\text{D5})$$

Then, substituting Equation (D5) to (D2), we reach the desired expression for  $\delta a_B$  on  $a_{B(\mathcal{R}=1)}$  as follows:

$$\frac{\delta a_B}{a_{B(\mathcal{R}=1)}} \simeq \frac{\ln E_c}{2 \ln(8B_0/B_{\text{Stev}})} \delta \beta. \quad (\text{D6})$$

Equation (D6) allows us to assign an uncertainty to  $a_{B(\mathcal{R}=1)}$ , and the relevant question is whether  $a_{B(\mathcal{R}=1)} \neq 1.6$  beyond this uncertainty. In this case, our conclusion on  $\mathcal{R}$  is unlikely to change. In addition, if  $\mathcal{R} > 1$  and  $a_{B(\mathcal{R}=1)} > 2$ , then  $a_{B(\mathcal{R}=1)}$  may be deemed unrealistic because the ICME magnetic field is required to fall more abruptly in the astrosphere than the ‘‘unobstructed’’  $a_B = 2$  case for the near-star CME expansion in order to achieve  $\mathcal{R} = 1$ . If  $a_{B(\mathcal{R}=1)} > 2$  beyond the applicable uncertainties, then our conclusion for  $\mathcal{R} > 1$  is considered solid, whereas in case  $|a_{B(\mathcal{R}=1)} - 2| \leq \delta a_B$ , our conclusion is again unlikely to change, but it is conceivable that  $\mathcal{R} \leq 1$  for a significantly steeper than 1.6 decrease of the ICME magnetic field in the astrosphere.

Figure 7 provides two examples of the ratio  $(\delta a_B/a_{B(\mathcal{R}=1)})$  of Equation (D6) for a wide range of superflare energies and Stevenson planetary fields, from zero to the  $B_{\text{Stev}}$  value for Earth ( $B_{\text{Stev}_{\oplus}} \simeq 0.309 \text{ G}$ ). Examples are based on two nominal  $B_0$  values, one for  $E_c = 10^{33} \text{ erg}$  (Figure 7(a)) and another for  $E_c = 10^{34} \text{ erg}$  (Figure 7(b)). These are mean values stemming from the Monte Carlo simulations of Figure 4 for these two energies. Both are toward the upper end of the distribution for near-Sun CME magnetic fields as found in Patsourakos & Georgoulis (2016). Stronger  $B_0$  increases the value of  $a_{B(\mathcal{R}=1)}$  (Equation (D1)) but correspondingly decreases its uncertainty fraction (Equation (D6)).

As an example, for the strong terrestrial magnetic field, we find  $a_{B(\mathcal{R}=1)} = 0.40 \pm 0.63$  (Equations (D1) and (D6)) assuming  $E_c = 10^{33} \text{ erg}$  and a nominal  $r_0 = 10 R_{\odot}$ . The respective value for  $E_c = 10^{34} \text{ erg}$  is  $a_{B(\mathcal{R}=1)} = 0.63 \pm 0.64$ . These are both very flat  $a_B$  values, flatter beyond the uncertainties than the nominal  $a_B = 1.6$  that gives  $\mathcal{R} \simeq 0.026$  and  $\simeq 0.052$ , respectively, under the same settings.

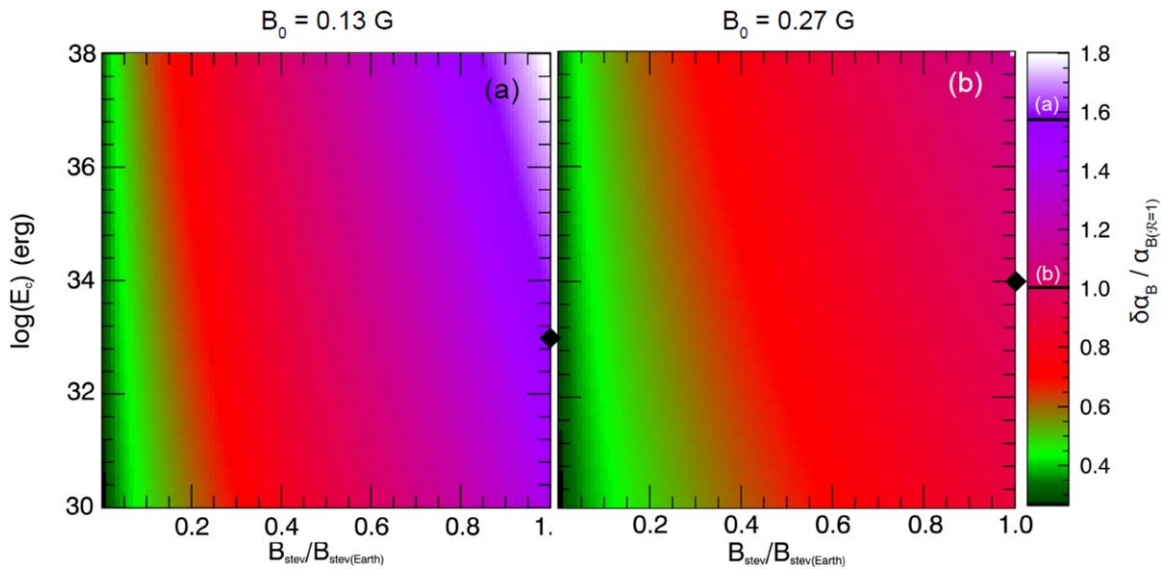


**Figure 7.** Normalized uncertainties ( $\delta a_B / a_{B(R=1)}$ ) of the radial power-law falloff index  $a_B$  required for an equipartition ( $\mathcal{R} = 1$ ) between the ICME and planetary magnetic pressures at a planetocentric distance equal to two planetary radii. The  $B_0$  values shown correspond to the mean near-Sun CME axial magnetic fields (Figure 4) for  $E_c = 10^{33}$  erg (a) and  $E_c = 10^{34}$  erg (b). Diamonds in the images and indications in the color bar show ( $\delta a_B / a_{B(R=1)}$ ) for Earth for the two cases.

### ORCID iDs

Evangelia Samara <https://orcid.org/0000-0002-7676-9364>  
 Spiros Patsourakos <https://orcid.org/0000-0003-3345-9697>  
 Manolis K. Georgoulis <https://orcid.org/0000-0001-6913-1330>

### References

- Airapetian, V. S., Barnes, R., & Cohen, O. 2020, *IJAsB*, 19, 136  
 Argiroffi, C., Reale, F., Drake, J. J., et al. 2019, *NatAs*, 3, 742  
 Armstrong, D. J., Pugh, C. E., Broomhall, A. M., et al. 2016, *MNRAS*, 455, 3110  
 Barabash, S., Fedorov, A., Lundin, R., & Sauvaud, J.-A. 2007, *Sci*, 315, 501  
 Berger, M. A. 1984, *GApFD*, 30, 79  
 Busse, F. H. 1976, *PEPI*, 12, 350  
 Carrington, R. C. 1859, *MNRAS*, 20, 13  
 Chapman, S., & Ferraro, V. C. A. 1930, *Natur*, 126, 129  
 Chen, H., Zhan, Z., Youngblood, A., et al. 2020, *NatAs*, in press  
 Christensen, U. R. 2010, *SSRv*, 152, 565  
 Donati, J. F., & Brown, S. F. 1997, *A&A*, 326, 1135  
 Garraffo, C., Drake, J. J., Cohen, O., Alvarado-Gómez, J. D., & Moschou, S. P. 2017, *ApJL*, 843, L33  
 Georgoulis, M. K., & LaBonte, B. J. 2007, *ApJ*, 671, 1034  
 Georgoulis, M. K., Tziotziou, K., & Raouafi, N.-E. 2012, *ApJ*, 759, 1  
 Griebmeier, J. M., Stadelmann, A., Penz, T., et al. 2004, *A&A*, 425, 753  
 Howard, R. A. 2006, *GMS*, 165, 7  
 Howard, R. A., Moses, J. D., Vourlidas, A., et al. 2008, *SSRv*, 136, 67  
 Howard, W. S., Tilley, M. A., Corbett, H., et al. 2018, *ApJL*, 860, L30  
 Jakosky, B. M., Grebowsky, J. M., Luhmann, J. G., et al. 2015, *Sci*, 350, 0210  
 Kane, S. R., Roettenbacher, R. M., Unterborn, C. T., Foley, B. J., & Hill, M. L. 2020, *PSJ*, 1, 36  
 Kay, C., Opher, M., & Kornbleuth, M. 2016, *ApJ*, 826, 195  
 Khodachenko, M. L., Ribas, I., Lammer, H., et al. 2007, *AsBio*, 7, 167  
 Koppurapu, R. K., Ramirez, R., Kasting, J. F., et al. 2013, *ApJ*, 765, 131  
 Lammer, H., Lichtenegger, H. I. M., Kulikov, Y. N., et al. 2007, *AsBio*, 7, 185  
 Lundin, R., Barabash, S., Andersson, H., et al. 2004, *Sci*, 305, 1933  
 Lynch, B. J., Airapetian, V. S., DeVore, C. R., et al. 2019, *ApJ*, 880, 97  
 Maehara, H., Shibayama, T., Notsu, S., et al. 2012, *Natur*, 485, 478  
 Manchester, W., Kilpua, E. K. J., Liu, Y. D., et al. 2017, *SSRv*, 212, 1159  
 Melosh, H. J., & Vickery, A. M. 1989, *Natur*, 338, 487  
 Mizutani, H., Yamamoto, T., & Fujimura, A. 1992, *AdSpR*, 12, 265  
 Moraitis, K., Tziotziou, K., Georgoulis, M. K., & Archontis, V. 2014, *SoPh*, 289, 4453  
 Moschou, S.-P., Drake, J. J., Cohen, O., et al. 2019, *ApJ*, 877, 105  
 Ngwira, C. M., Pulkkinen, A., Kuznetsova, M. M., & Glocer, A. 2014, *JGRA*, 119, 4456  
 Nieves-Chinchilla, T., Vourlidas, A., Raymond, J. C., et al. 2018, *SoPh*, 293, 25  
 Nindos, A., Zhang, J., & Zhang, H. 2003, *ApJ*, 594, 1033  
 Patsourakos, S., & Georgoulis, M. K. 2016, *A&A*, 595, A121  
 Patsourakos, S., & Georgoulis, M. K. 2017, *SoPh*, 292, 89  
 Patsourakos, S., Georgoulis, M. K., Vourlidas, A., et al. 2016, *ApJ*, 817, 14  
 Petit, P., Dintrans, B., Solanki, S. K., et al. 2008, *MNRAS*, 388, 80  
 Raghav, A. N., & Shaikh, Z. I. 2020, *MNRAS*, 493, L16  
 Russell, C. T., Le, G., Chi, P., et al. 2000, *AdSpR*, 25, 1369  
 Sakurai, T. 1981, *SoPh*, 69, 343  
 Salman, T. M., Winslow, R. M., & Lugaz, N. 2020, *JGRA*, 125, e27084  
 Sano, Y. 1993, *JGG*, 45, 65  
 Schulze-Makuch, D., Méndez, A., Fairén, A. G., et al. 2011, *AsBio*, 11, 1041  
 Stevenson, D. J. 2003, *E&PSL*, 208, 1  
 Stevenson, D. J., Spohn, T., & Schubert, G. 1983, *Icar*, 54, 466  
 Sulis, S., Lendl, M., Hofmeister, S., et al. 2020, *A&A*, 636, A70  
 Thernisien, A. 2011, *ApJS*, 194, 33  
 Thernisien, A., Vourlidas, A., & Howard, R. A. 2009, *SoPh*, 256, 111  
 Tziotziou, K., Georgoulis, M. K., & Liu, Y. 2013, *ApJ*, 772, 115  
 Tziotziou, K., Georgoulis, M. K., & Raouafi, N.-E. 2012, *ApJL*, 759, L4  
 Vanderspek, R., Huang, C. X., Vanderburg, A., et al. 2019, *ApJL*, 871, L24  
 Vida, K., Kóvári, Z., Pál, A., Oláh, K., & Kriskovics, L. 2017, *ApJ*, 841, 124  
 Vidotto, A. A., Jardine, M., Opher, M., Donati, J. F., & Gombosi, T. I. 2011, *MNRAS*, 412, 351  
 Villarreal D'Angelo, C., Jardine, M., Johnstone, C. P., & See, V. 2019, *MNRAS*, 485, 1448  
 Vourlidas, A., Balmaceda, L. A., Stenborg, G., & Dal Lago, A. 2017, *ApJ*, 838, 141  
 Vourlidas, A., Lynch, B. J., Howard, R. A., & Li, Y. 2013, *SoPh*, 284, 179  
 Zendejas, J., Segura, A., & Raga, A. C. 2010, *Icar*, 210, 539  
 Zurbuchen, T. H., & Richardson, I. G. 2006, *SSRv*, 123, 31